An Investigation into the Design of Surface Piercing Super Cavitating Hydrofoils

Submitted for consideration in the
2017 IHS Mandles Prize Competition

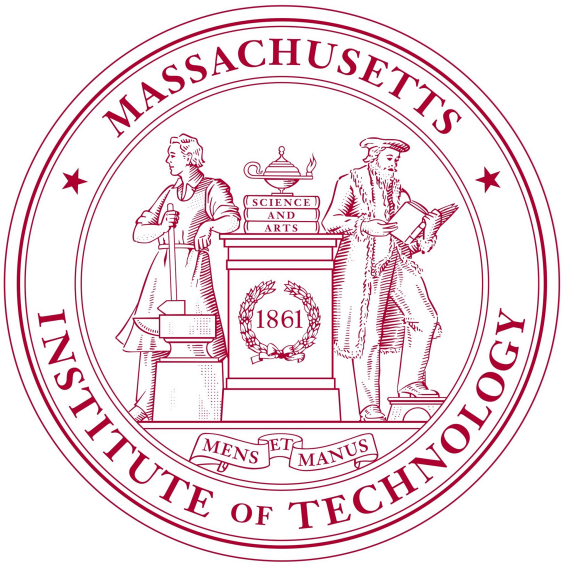

Timothy Dutton, LCDR USN

Department of Mechanical Engineering
Massachusetts Institute of Technology
77 Massachusetts Avenue, Cambridge, MA USA
Phone (757)343-3737 E-mail
www.mit.edu

supervised by
Dr. Stefano Brizzolara

ABSTRACT

The fluid-dynamic design of hydrofoils to support marine crafts at high speeds has received growing interest in recent years. Theoretical, physical, and numerical methods for the design of high speed hydrofoils belong to disciplines at the intersection between naval architecture and aeronautical engineering. Physics involved in the design of high-speed surface-piercing hydrofoils is complex involving three different fluid phases (air, water and vapor) and complex fluid dynamic mechanisms like unsteady cavitation and ventilation and their interaction.

For speeds considerably higher than the incipient cavitation speed, the hydrofoil sections need to be adapted and design to exploit cavitation instead of avoiding it. This is particularly true for surface piercing hydrofoils that in addition to cavitation are affected by ventilation from the free surface.

The paper presents main results of an investigation into the relative formation of ventilation and cavitation regions of surface piercing super cavitating hydrofoils (SPSCHs), with special attention to the effects of cavitation number. The relative size and location of the ventilation and cavitation regions have significant contributions to the hydrodynamic properties of the SPSCHs, in particular lift and drag forces.

A series of 3D multi-phase Reynold Averaged Navier-Stokes Equation (RANSE) simulations of varying cavitation number reveal the dependence of the ventilation and cavitation regions on the cavitation number, angle of attack, and distance from the free surface. The RANSE simulations are validated against an analytical estimate based on an appropriate lifting line method at near zero cavitation numbers, and against empirical results obtained through tow tank testing at higher cavitation numbers. The analytical and empirical validation bound the range of cavitation numbers considered in this study from $\sigma = 0.05$ to $\sigma = 2.37$.

Previous studies attempting to predict the performance of SPSCHs using a viscous lifting line (VLL) method have not taken the effects the free surface into account. As such, they sufficiently far away from the free surface such that ventilation will not occur. A modified version of these VLL methods, informed by the effects of cavitation number presented here, would allow for the more general application of the VLL to SPSCHs.

Timothy Dutton, LCDR USN
Massachusetts Institute of Technology

An Investigation into the Design of Surface-Piercing Super-Cavitating Hydrofoils

1 Abstract

The fluid-dynamic design of hydrofoils to support marine crafts at high speeds has received growing interest in recent years. Theoretical, physical, and numerical methods for the design of high speed hydrofoils belong to disciplines at the intersection between naval architecture and aeronautical engineering. Physics involved in the design of high-speed surface-piercing hydrofoils is complex involving three different fluid phases (air, water and vapor) and complex fluid dynamic mechanisms like unsteady cavitation and ventilation and their interaction.

For speeds considerably higher than the incipient cavitation speed, the hydrofoil sections need to be adapted and design to exploit cavitation instead of avoiding it. This is particularly true for surface piercing hydrofoils that in addition to cavitation are affected by ventilation from the free surface.

The paper presents main results of an investigation into the relative formation of ventilation and cavitation regions of surface piercing super cavitating hydrofoils (SPSCHs), with special attention to the effects of cavitation number. The relative size and location of the ventilation and cavitation regions have significant contributions to the hydrodynamic properties of the SPSCHs, in particular lift and drag forces.

A series of 3D multi-phase Reynold Averaged Navier-Stokes Equation (RANSE) simulations of varying cavitation number reveal the dependence of the ventilation and cavitation regions on the cavitation number, angle of attack, and distance from the free surface. The RANSE simulations are validated against an analytical estimate based on an appropriate lifting line method at near zero cavitation numbers, and against empirical results obtained through tow tank testing at higher cavitation numbers. The analytical and empirical validation bound the range of cavitation numbers considered in this study from $\sigma = 0.05$ to $\sigma = 2.37$.

Previous studies attempting to predict the performance of SPSCHs using a viscous lifting line (VLL) method have not taken the effects the free surface into account. As such, they sufficiently far away from the free surface such that ventilation will not occur. A modified version of these VLL methods, informed by the effects of cavitation number presented here, would allow for the more general application of the VLL to SPSCHs.

2 Introduction

The use of hydrofoils in high-speed vessels as a means of supporting the vessel's weight, either partially or fully, continues to proliferate throughout different designs of high speed marine craft. First used by Enrico Forlanini in 1906 as an experimental vessel, hydrofoil applications today appear in the military, commercial, and recreational arenas. Perhaps most prominently, inclusion of hydrofoils in the America's Cup, with rule change AC72, first displayed their benefits on the world stage in 2013 [1]. Hydrofoil supported vessels have numerous advantages when compared to traditional displacement or planing hulls when operating at high speeds. They enjoy reduced motions by drastically reducing wave excitation forces, as well as reduced frictional and wave-making resistance by drastically reducing the wetted surface area of the vessel and the volume of water displaced when operating at high speeds. The hydro-dynamic lifting force of the foils essentially eliminates the need to displace a large volume of water to generate the hydrostatic lifting force required for displacement vessels. When the foils are actively used as control surfaces, hydrofoil vessels also experience improved maneuverability. In application, hydrofoils can be

fully submerged or surface piercing, and also cover the sub-cavitating, super-cavitating, and the transitional regimes.

The genesis for this research is a grant by the Office of Naval Research (ONR), to optimize and design a "Vee" shaped surface-piercing hydrofoil for stabilizing a stepped planing hull by providing approximately 10% of the vessel's weight in lift. The design speed of the vessel, well in excess of 50 knots, necessitates super-cavitation on the foil.

The research presented here aims to improve the ability to design surface-piercing supercavitating hydrofoils (SPSCHs). In order to maximize the potential benefit of a specific hydrofoil through optimization, a method of rapidly predicting a hydrofoil's performance is required. Although increasingly accurate, three dimensional computational fluid dynamics (CFD) simulations are too computationally intensive to be useful in optimization where many configurations must be evaluated rapidly. As an alternative, lifting line methods can be run very quickly, and when properly configured have been shown to produce sufficiently accurate results [3]. The ability to iteratively evaluate foils allows for a numerical hydrodynamic optimization of design. The combination of speed and accuracy of the lifting line method makes it the only suitable option for foil optimization.

Prandtl's classical lifting line method, limited in applicability to inviscid flows and linear lift slopes, is not able to provide accurate results when modeling SPSCHs [4]. The Super-Cavitating condition results in the non-linearity of lift slope over the range of angles of attack encountered in operation [7]. Though not identical, this non-linear lift slope is similar to the lift slope of an airfoil operating near the stalling condition. Modified Lifting Line methods incorporating circulation based and angle of attack based corrections have been proposed in various non-linear lifting line methods to address airfoils operating at or past the stalling condition. [12] [13] [14]. Vernengo, Bonfiglio, and Brizzolara proposed a viscous lifting line method specifically created to analyze the hydrodynamic performance of a super-cavitating hydrofoil [3]. Their method is based on a three-dimensional numerical solution for a finite wing in inviscid flow proposed by Katz and Plotkin [11], and generalized to viscous flow through the inclusion of high fidelity two-dimensional multi-phase URANS simulations used to provide lift and drag data over the applicable range of angles of attack. Though accurate for fully submerged super-cavitating hydrofoils, their methods do not address the surface-piercing condition.

This paper generalizes the Viscous Lifting Line (VLL) method outlined by Vernengo et al. to incorporate the added complexity of a foil penetrating a free-surface boundary. An analysis of an appropriate method of images across the free-surface, effects of the disturbance of the free-surface by the motion of the hydrofoil, and the interaction between the ventilation region and cavitation bubble generated by the foil is provided.

3 Background

3.1 Lifting Line Theory

Lifting line theory, first developed by Prandtl, applied only to small disturbances on a wing in inviscid flow, and was used to model the characteristics of wings in air by solving for the the unknown circulation distribution of the wing[4]. Hydrofoils operate under the same assumptions of air wings only in a different fluid medium, so the same Lifting Line approach is applicable for modeling their hydrodynamic characteristics. Beginning with the Kutta-Joukowski theorem stating that "the lift per unit span is directly proportional to circulation",[15] as expressed in Equation 1, a wing is represented by a bound circulation, oriented and positioned such that it provides a lifting force at the aerodynamic center of the wing.

$$L' = \frac{1}{2}\rho_\infty V_\infty \Gamma \tag{1}$$

Because the wing is finite in length, and Helmholtz's Theorem requires that a vortex filament extends to infinity or forms a closed path, the vortex filament used to create the bound vortex must extend beyond the bounds of the wing. [15] Lifting Line theory addresses this requirement by bending and extending the ends of the vortex filament to infinity behind the wing. The horseshoe shaped vortex filament consists of a bound section, and two trailing sections, all required by Helmholtz to be of the same strength. [15]. The non-uniform lift distribution of a finite wing, and the Kutta con-

dition which requires the circulation to equal zero at the tips [15] requires a series of these horseshoes vortex filaments of varying strengths to be used to represent the lift distribution of the wing as shown in Fig. 1.

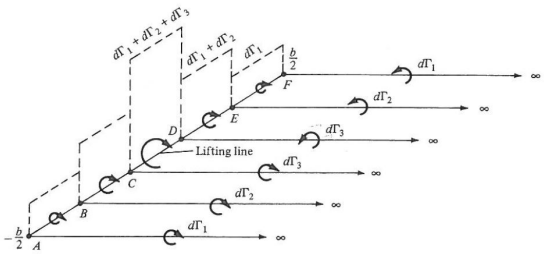

Figure 1: Example of circulation distribution on a wing. [15]

Each bound vortex and trailing vortex segment act to induce a down wash velocity at each point along the entire span of the lifting line ($v_i(x)$). The induced velocity, combined with the free stream velocity (V_∞) provides an effective velocity ($V_{eff}(x)$) which is the actual velocity vector present at that location along the span. The angle between the chord line and V_{eff} is defined as the effective angle of attack (α_{eff}) and describes the angle of attack the section of the foil is operating at.

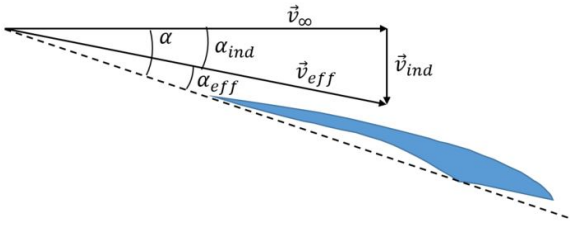

Figure 2: Graphical depiction of the velocities and angles of attack used in the description of Lifting Line Theory.

Next a solution for $\Gamma(y)$ can be obtained by applying a zero flow boundary condition normal to the wing's surface at a position of $\frac{3}{4}$ chord (referred to as collocation points) in accordance with a lumped vortex approximation. The boundary condition can be expressed as in Equation 2 simply stating that the summation of velocity components from the free-stream, and the bound and trailing vorticies normal to the collocation point must add to zero. Furthermore the v_{bound} is a function of $\Gamma(y)$ (Eq. 3) and $v_{trailing}$ a function of $\frac{d\Gamma(y)}{dy}$ over the span of the wing (Eq. 4) and are found respectively by applying the lumped-vortex model and the Biot-Savart law for a semi-infinite vortex.

$$V_\infty \cdot n + v_{bound} \cdot n + v_{trailing} \cdot n = 0 \tag{2}$$

$$v_{bound} = \frac{-\Gamma(y)}{2\pi[c(y)/2]} \tag{3}$$

$$\mathbf{v}_{trailing} = \frac{\Gamma}{4\pi} \int \frac{d\mathbf{l} \times \mathbf{r}}{|\mathbf{r}|^3} \tag{4}$$

Equations 3 and 4 combined with equation 2 provide the Prandtl lifting-line integro-differential equation allowing for $\Gamma(y)$ to be solved. From here the Lift and induced Drag (D_i) are found through application of the Kutta-Joukowski theorem Eq. 1.

The placement of the collocation point (X_c) at the $\frac{3}{4}$ chord location is accurate for sub-cavitating flows where a constant lift slope value of 2π exists [15]. However, a super-cavitating hydrofoil does not exhibit a linear lift slope at typical angles of attack. When operating at lower angles of attack a lift slope of 2π is observed, but at higher angles a transition to a lift slope of $\frac{\pi}{2}$ exists (Illustrated in Fig. 3). The value of the cavitation number affects the angle of attack where this transition in lift slope occurs with lower cavitation numbers corresponding to a transition at lower angles of attack [7]. As a result of the non-linear lift slope, the position of the collocation point is also variable. Equation 5 provides a formula for calculating the position of the collocation point as a function of the chord length. The method can be further generalized to incorporate viscous drag by including the sectional 2D data across the range of effective angles of attack acting on the wing.

$$X_c = \frac{1}{4\pi}(\pi + \frac{\delta C_L}{\delta \alpha}) \tag{5}$$

A series of 2D CFD simulations, or cavitation tunnel testing, is required to obtain accurate data to determine $\frac{\delta C_L}{\delta \alpha}$ over the range of applicable angles. This is a time intensive process, but is only

required to be conducted once for each 2D foil cross-section used in design of the foil.

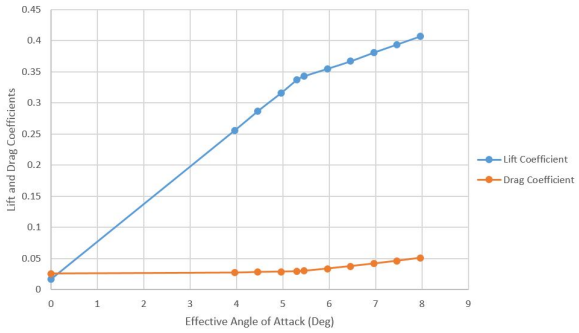

Figure 3: Lift and Drag coefficient distribution of SCSB profile

Previous VLL methods, although accurate and useful in most situations, do not account for the effects of the free-surface present with a surface-piercing hydrofoil. The close proximity of a free-surface provides a number of added layers of complexity. First, a method of images must be used to accurately calculate the disturbance induced by the nearby free-surface boundary. Molland and Turnock show that at low, near zero, Fr, a symmetric image, similar to that expected across a rigid wall, is appropriate, since the shape of the free-surface is not affected by the hydrofoil. Conversely, at high Fr (> 1) an anti-symmetric image, like that used in biplane analysis, is required. [6] Secondly, the motion of the foil through the liquid creates a disturbance of the free-surface. The shape of the free-surface is assumed to approximate the shape of the back of the foil. This results in a build up on the face of the foil. Lastly, there will be an interaction between a ventilated region, created by the free-surface distortion and consisting entirely of air at atmospheric pressure, and a cavitation bubble, isolated from the atmosphere by the foil and a layer of fluid, which is at vapor pressure. None of these effects are directly addressed in previous VLL methods, but are critical to the accurate prediction of a surface piercing super cavitating hydrofoil. The design process used in the creation of foils built and tested for this paper addresses only the method of images directly. Analysis of the testing results provides insight into the effects of the others.

3.2 The SCSB Profile

Super-Cavitating hydrofoils fundamentally differ from a traditional NACA profile in their hydrodynamic modes of operation. Figure 4 shows the progression of flow conditions with decreasing cavitation number (σ) as defined in Eq. 7. At sufficiently high σ a foil is fully wetted when no low pressure regions exist where the local pressure is less than the vapor pressure of the fluid. Foils designed to operate in this condition are free of any discontinuities in surface normals with the exception of at the trailing edge. At the trailing edge, in order to satisfy the Kutta condition, if there is a finite angle, then a stagnation point exists and the fluid velocity is zero, in the event of a cusped trailing edge the velocities on both the face and back are equal in magnitude and direction, in no cases is flow separation present anywhere along the foil. For a fully wetted foil, lift is generated through a difference in fluid flow speed over the top and bottom of the foil creating a pressure differential in accordance with Bernoulli's equation.

$$\sigma = \frac{p_o - p_v}{\frac{1}{2}\rho V^2} \tag{6}$$

As σ drops, the low pressure region on the top of the foil begins to approach the vapor pressure of the fluid. Once the σ is sufficiently low for local pressures to drop below the vapor pressure, a region of cavitation beings to form. Starting with a number of individual bubbles during the incipient cavitation condition, and progressing until the super-cavitating condition, which is marked by a vapor of air cavity region forming in the region down steam of the foil. For a foil designed to operate fully wetted (i.e. a NACA profile) the super-cavitating condition corresponds to a significant increase in drag as a large low pressure region forms behind the foil. Foils designed to operate at such low cavitation numbers are characterized by a sharp leading edge, specifically designed to induce flow separation at the Leading Edge creating a region of low pressure (the vapor pressure of the fluid) along the entire back of the foil.

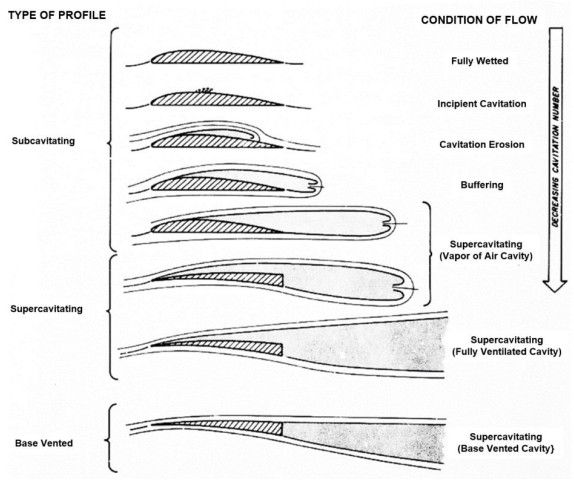

Figure 4: Depiction of traditional and supercavitating hydrofoil cross-sections and the development of cavitation regions on them at various ranges of σ. [19]

The traditional designs shown in Fig. 4 for both the fully wetted and the super-cavitating conditions perform poorly when operating outside of their designed operating condition. The specific 2D foil analyzed in this research was specifically designed for improved hydrodynamic performance at both low and high σ [7]. The class of foils from which it is derived are collectively referred to as SCSB hydrofoils and contain a number of unique design characteristics. When operating at low σ values, the foil performs like a traditional super-cavitating foil with a sharp leading edge, and a discontinuity in surface normal on the face of the foil where the trailing edge typically would be.

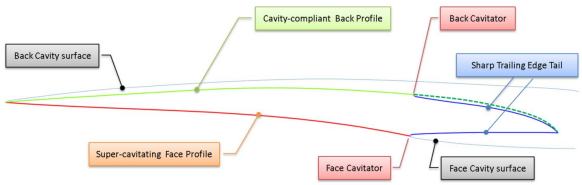

Figure 5: Component description of SCSB profile [16]

This results in the foil having the same wetted area in operation as a traditional foil without the trailing edge tail which is completely enclosed in the vapor of air cavity for the SCSB foil because the kink along the face of the foil induces flow separation. When operating at high σ values the sharp trailing edge tail allows for the flow which separated at the face and back cavitators to reconnect to the foil and regain much of the hydrodynamic efficiency lost with traditional super-cavitating profile shapes. This family of foil design has been shown to demonstrate nearly identical hydrodynamic efficiency to traditional super-cavitating profiles at low σ values, and roughly triple their hydrodynamic efficiency at high cavitating numbers. [7]

4 Tow Tank Testing

4.1 Optimal Foil Design

Using the methods described in Section 3.1, the 2-Dimensional profile described in Section 3.2, and a differential evolution algorithm [8] to optimize the span-wise angle of attack distribution with the objective of minimizing the total Lift and Drag on the foil, an optimal foil was designed. The results of a series of 2-Dimensional multi-phase URANS simulations used to determine the local lift slope at each angle of attack are found in Fig. 3. Figure 6 shows the volume of flow present on the foil at various angels of attack.

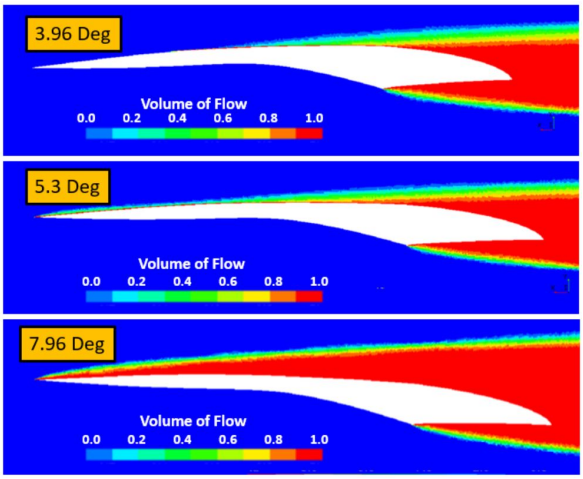

Figure 6: Collection of images showing the Volume of Flow distribution over the SCSB profile at various angles of attack all at a cavitation number of $\sigma = 0.05$.

Across the range of angles of attack presented in Fig. 6, the foils all behave as expected for a super cavitating hydrofoil. In each case the face of the foil is fully wetted up to the designed face cavitator, generating a positive lifting pressure, while a portion of the back of the foil is experiencing atmospheric pressure. At angles less then 5.3 degrees, a significant portion of the back of the foil remains wetted. These angles of attack also correspond to the traditionally expected lift slope of 2π. At angles of attack greater than 5.3 degrees, a cavity

formed at the leading edge fully encapsulates the back face of the foil. These angles of attack correspond to a much shallower lift slope of $\frac{\pi}{2}$. This transition in lift slope, shown in Fig. 3 is what creates the non-linearity precluding the application of Prandtl's classical lifting line theory. It is the difference in pressure between the face and back which generates the lift. In each case also, the cavity formed on the back of the foil extends behind the foil, creating a large low pressure region, causing the significant drag which is unavoidable for a super-cavitating foil. The pressure distribution along the face of the foil is plotted in Fig. 7.

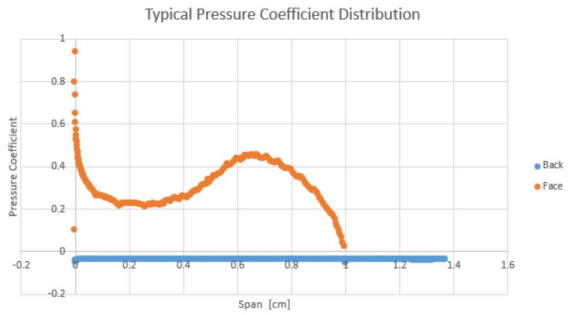

Figure 7: Typical distribution of pressure along the face of a 2-D foil section at $\sigma = 0.05$.

The optimization algorithm only optimizes the angle of attack distribution along the span of the foil, not the geometric shape of the foil itself. The shape must be provided by the user. The foil considered here is of a "Vee" shape design, with a span of 7.2cm on each side, a constant chord and no sweep angle. A further constraint imposed, is that the foil must provide 83.94 N of vertical lift at a speed of 11.1 m/s.

4.2 Testing and Results

Following design, the optimal foil was constructed with a Computer Numerical Control (CNC) machine at the MIT Central Machine Shop and tested on the high-speed carriage at the United States Naval Academy (USNA). The tow tank testing results, and a comparison to the results expected from the design process are detailed in this section.

The USNA hydromechanics laboratory's high speed tow tank is 380ft in length, 26ft in breadth, 16ft deep, and has a maximum usable carriage speed of 30 ft/s over a total carriage travel of 270ft. The available carriage speed permitted testing the foil at near design speed (design speed is 36.6 ft/s). The mounting mechanism provided for the manual adjustment of angle of attack through the placement of a pin in pre-drilled holes. A basic schematic of the mount used is shown in Fig. 8

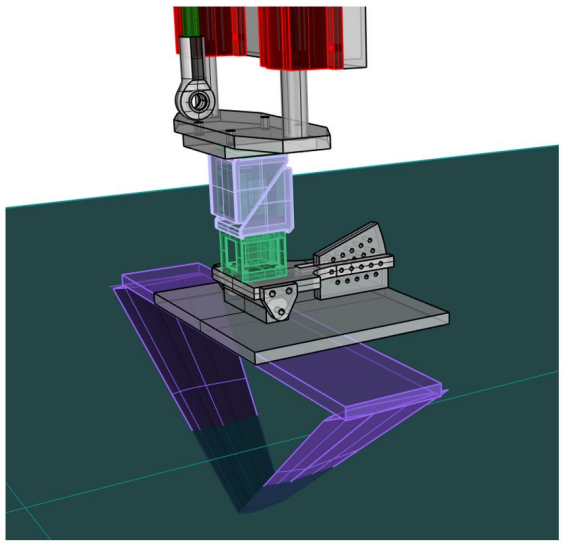

Figure 8: Basic configuration of the mounting mechanism used in tow tank testing.

Tests were run at varying angles of attack at the maximum carriage speed of 30 ft/s. The results were then scaled down by the ratio of testing and design speeds squared, $(\frac{30ft/s}{36ft/s})^2$, to provide an accurate comparison to the expected results from the design.

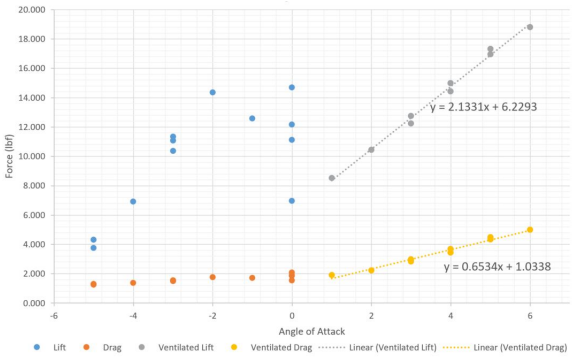

Figure 9: Basic configuration of the mounting mechanism used in tow tank testing.

The results show that two clear operating conditions exist. A linear trend exists at lower angles of attack, and a separate linear trend exists at higher angles of attack. Between these two regions

of stable linear trend, a region of instability exists with no clear trend. The linear trend at low angles of attack corresponds with a stable condition where the flow over the back of the foil remains attached (See Fig. 10). Conversely, the linear trend at high angles of attack corresponds with a stable condition where the back of the foil is fully ventilated. (See Fig. 11). For the region in between, the portion of the foil which remains attached is variable and unstable. This instability resulted in multiple runs at the same angle of attack yielding a wide range of results bound by the two linear trend lines as shown in Fig 9 at zero degrees. Visual observation of the foil in motion demonstrated varying degrees of attached flow, and in some cases non-symmetric ventilation across the foil.

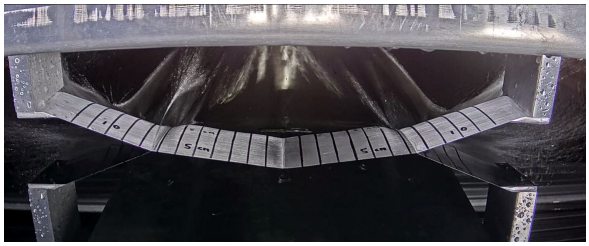

Figure 10: Flow depicted is fully attached along the back of the foil. The spray off the leading edge is visible coming off the leading edge of the foil around the design free-surface and the back of the foil is visible and un-augmented through a flat free surface.

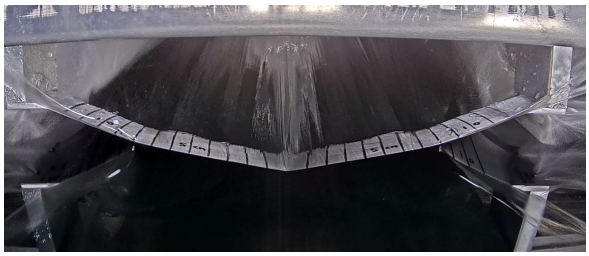

Figure 11: Flow depicted is fully ventilated. The sheet of water coming off the leading edge is visible along the entire span and the back of the foil is visibly augmented being viewed through a non-uniform spray.

Froude scaling between the model and full scale foil was maintained, but due to the inability to control ambient pressure in the testing facility it was not possible to maintain the cavitation number σ (Eq. 7) between the model and full scale foil. The variance in σ prevented the foil from being fully ventilated at zero degrees angle of attack as would be expected if operating at full scale. To compare the experimental results to those expected, the linear trend of the fully ventilated foils is extrapolated to zero degrees angle of attack.

$$\sigma = \frac{p_{amb} - p_v}{\frac{1}{2}\rho v^2} \tag{7}$$

5 Discussion of the Results

It was expected before testing that there would be some amount of error between the expected and actual results due to several factors related to a surface piercing foil: the unknown level of the free-surface perturbed by the foil; the simplified methods of images to represent the free-surface effect, and the un-modeled interaction between ventilation and cavitation regions. This section provides a brief investigation into each of these potential sources of error.

5.1 Potential Sources of Error

5.1.1 Physical Defect During Construction

The first potential source of error which had to be addressed concerned the potential for a physical deviation between the designed foil, and the foil which was physically tested. Any deviation from the design dimensions would produce a change in the foil's hydrodynamic performance, and invalidate all of the testing data. Creating a 3D RANSE simulation, run at the tow tank testing conditions, with the same CAD model of the foil used in design, provided a means of verifying the physical model's dimensions.

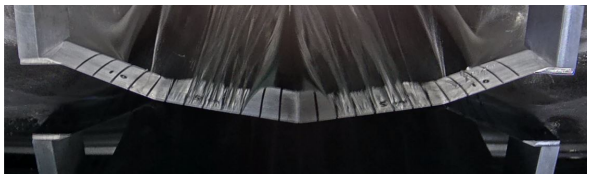

Figure 12: Image of optimal during tow tank testing at zero degrees angle of attack

Visual inspection of the simulation results show a similar flow distribution over the back of the foil in both the two tank tests (Fig. 12), and computer simulation (Fig. 13). Each flow pattern demonstrates a foil fully ventilated near the free surface, characterized by the spray from the foils' leading

edge, transitioning to a fully wetted condition near the foils' tip. The measured lift from the CFD simulation (9.4 lbf) also falls within the range of results from the towing tank (7-15 lbf). The similarities in flow pattern, and agreement in measured forces, support the argument that physical model dimensions match the design foil. Therefore, the discrepancies between expected and actual test results must be somewhere in the modeling process used to design the foil.

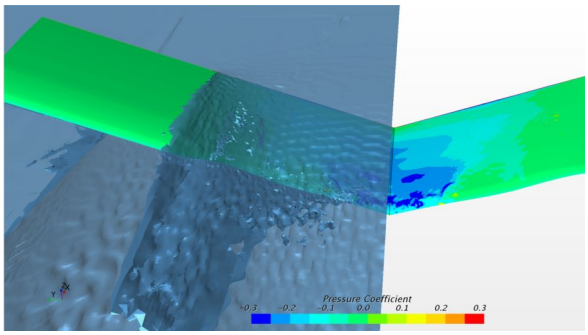

Figure 13: Image of flow on back of foil from CFD simulation run at Sigma = 2.37

5.1.2 Free-Surface Effect (Bi-Plane versus Rigid Wall)

A critical assumption made in the design of the foil was how the circulations used in the lifting line code are mirrored across the free-surface. It is known that the perturbation effect of the free-surface on a surface piercing hydrofoil varies with speed. Molland and Turnock present a relationship between effective aspect ratio (AR_e) and Froude number based on the foil chord F_c. At near zero Froude numbers the AR_e is nearly doubled and at higher Froude numbers it is effectively halved. [6]

At low speeds, the AR_e is 2, as would be the case in a perfectly reflected wing across a rigid wall. As the speed increases, the AR_e drops past a value of 1 (No reflected images) at a Froude number of 0.8, then appears to approach 0.5 asymptotically as the Froude number continues to increase. The Froude number of Foil #1 is 15.8 corresponding to an AR_e of approximately 0.5. To test the appropriateness of using the anti-symmetric method of images, an analysis of the foil under the same VLL method used in design, but with variation in method of images applied was conducted. In execution, both the symmetric and antisymmetric images are calculated. A weighting factor (w), ranging from purely symmetric images at a value of 0 and fully antisymmetric at a value of 1 is used. In between these two extremes, both images are used but the velocities induced by the anti-symmetric images are weighted by the factor w, while those induced by the symmetric images are weighted by (1-w). Results of the analysis are contained in Fig.15, and show the transition from a fully symmetric, to fully anti-symmetric method of images through the application of a weighted averages. When compared to a RANSE simulation run at the design conditions, the analysis model with weighting factor $w = 1$ (fully anti-symmetric) produces a lift coefficient within 1% of the CFD model. Additionally, the transition between the two extremes loosely resembles the transition of AR_e from 2 to 0.5 predicted with a change in Froude number predicted by Molland and Turnock indicating that the transition from symmetric to anti-symmetric images is a fair approximation of the transition of AR_e from values of 2 to 0.5. This also indicates that any deviation from the fully anti-symmetric method yields less accurate results.

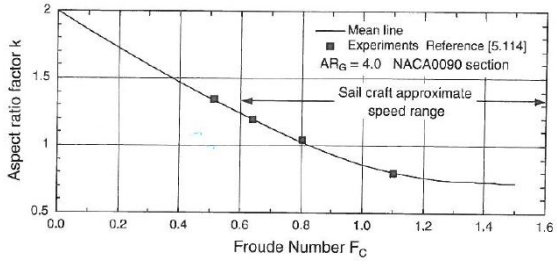

Figure 14: Plot of AR_e versus F_c showing at very low Froude numbers.

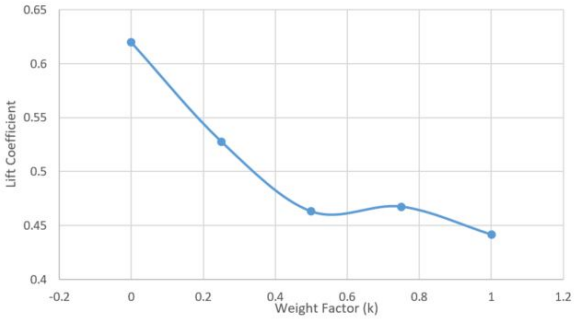

Figure 15: Plot of lift coefficient versus weighting factor (k).

5.1.3 Level of the Disturbed Free Surface

In design, an undisturbed free-surface held constant at the design span of 7.2 cm is enforced. In operation, this assumption does not hold. A real foil in motion can not be treated as a thin plate and necessarily creates a disturbed free-surface. This difference in conditions of the free-surface between how the foils are modeled and the realities of operation present in testing, results in differences in expected and measured forces. This section attempts to classify the sources of differences attributable to the disturbed free-surface, and to propose a method to model them.

The level of disturbed free-surface acts in two separate ways to change the hydrodynamic forces acting on the foil. Along the face of the foil, an additional wetted area forms, similar to the development of a spray root line on the pressure face of a planing hull [18]. The additional area is defined by a triangular region extending from the design water level of the foil to the new water line which exists from the leading edge at the design water line to the trailing edge at an angle ψ. The angle ψ is a function of the dihedral angle θ and local angle of attack α_{geom}:

$$\psi = tan^{-1}\left(\frac{\pi}{2}\frac{tan\alpha_{geom}}{tan\theta}\right) \tag{8}$$

Dynamic forces acting on this additional wetted area provide a positive pressure on the face of the foil while the back of the foil in this area remains at atmospheric pressure, the result is an additional lifting force. Through measuring the forces from the CFD simulation on only the area of the foil defined by the designed area, $Lift_{design}$ (from the tip of the "Vee" up to the design span of 7.2cm) and comparing it to the forces from the entire foil $Lift_{total}$, the lift from the additional wetted area $Lift_{add}$ is found by:

$$Lift_{add} = Lift_{total} - Lift_{design} \tag{9}$$

The lift coefficient of the additional wetted area is found by:

$$C_{L_{add}} = \frac{Lift_{Add}}{\frac{1}{2}\rho v^2 A_{Add}} \tag{10}$$

$$A_{Add} = c^2 * tan(\psi) \tag{11}$$

The value of $C_{L_{add}}$ is roughly 3.6 times the value of the lift coefficient of the foil at the design free surface:

$$C_{L_{add}} = 3.6 * C_{L_{DFS}} \tag{12}$$

It is then possible to estimate the additional lift from the disturbed free-surface by combining equations 8, 12, and 11. :

$$Lift_{Add} = \frac{1}{2}\rho v^2 (3.6 * C_{L_{DFS}})(c^2\left(\frac{\pi}{2}\frac{tan\alpha_{geom}}{tan\theta}\right)) \tag{13}$$

Equation 13 provides a corrections factor to be added to the lift calculated on the design span only.

A second effect of this additional wetted area created by the disturbed free surface is the shape of the lift distribution along the wing span. A gradual transition from a lift maximum somewhere along the middle of the wing to zero at the root is typically expected [15], as shown in Fig. 16. Because it was known that the end of the wing span where lift equals zero would not be at the design free-surface, but at the true free-surface created by the displaced water acting on the foil, the optimization code forced the circulation at the design free surface to be no less than 10% of the maximum circulation value. If this constraint is too restrictive or too liberal, the optimization code would have forced the circulation values, and there for the induced velocities and design angles of attack, to not be optimal.

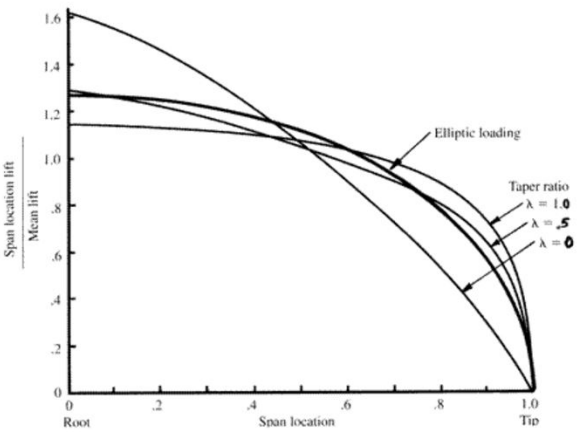

Figure 16: Typical lift distribution along a wing span from root to tip.

Investigating the lift distribution on the foil from a CFD simulation revealed that over the design span of the foil, the lift is essentially constant and the transition to zero lift occurs almost entirely on the additional wetted span of the foil created

by the disturbed free surface (Fig. 17). This indicates the a future VLL method should constrain the limitations on circulation to values much closer to the maximum circulation than the 10 % constraint used here.

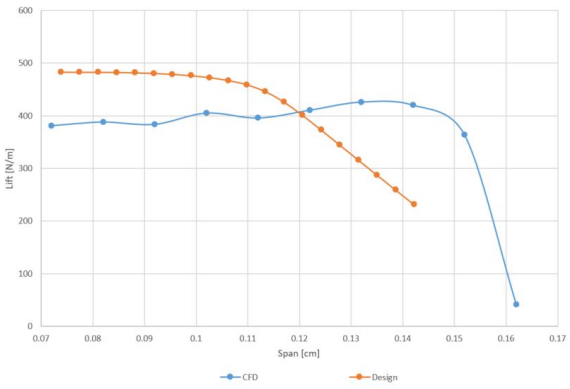

Figure 17: Comparison of lift distribution between design and CFD

5.1.4 Effect of Cavitation Number

In order to gain a stronger understanding of the effects of the cavitation number σ on foil operation a second CFD simulation at the design σ of 0.05 was run. The RANSE simulation of the optimal foil run at the conditions matching those of the tow tank testing ($\sigma = 2.37$) is compared to a simulation run at the design condition ($\sigma = 0.05$). Pressure distribution along identical 2D chord-wise cross-sections of each foil reveal a fundamental difference in hydrofoil operation. For σ=2.37, directly aft of the kink on the face of the foil there is a region of negative pressure, indicating that this region is not ventilated (Fig. 18). The sectional data used to calculate the $\frac{\delta C_L}{\delta \alpha}$ used in the design of the foils instead were fully ventilated aft of the kink (Fig. 19). The negative pressure on the face of the foil, clearly results in a reduced lift, and therefore a strong candidate for the difference in lift between the design and experiment.

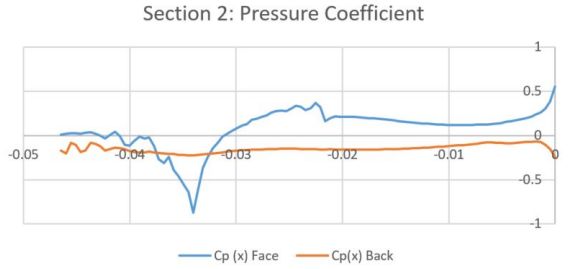

Figure 18: Pressure distribution on foil 1 cross section at $\sigma = 2.37$

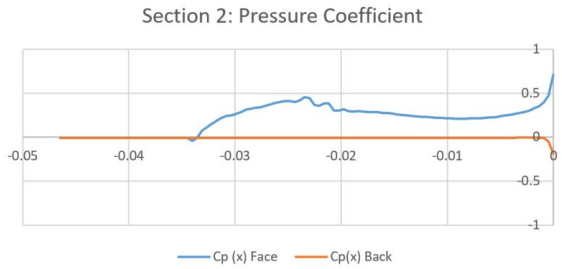

Figure 19: Pressure distribution on foil 1 cross section at $\sigma = 0.05$

Negative pressure aft of the kink indicates that this portion of the foil is at least partially wetted, with a shed vortex creating an area of low pressure there, but not sufficient to induce cavitation. The failure of this region to ventilate is related to a difference in cavitation number σ:

$$\sigma = \frac{p_{amb} - p_v}{\frac{1}{2}\rho v^2} \tag{14}$$

When adjusted for the change in deformed free-surface by only considering the portion of the foil below the undisturbed free-surface, the $\sigma_0 = 0.05$ simulation agrees with the expected design results within 1%, ultimately validating the VLL method with free-surface corrections.

The two runs are identical in all respects except for the change in ambient pressure, acting to lower the cavitation number. This indicates a dependence of the pressure distribution, and therefore the hydrodynamic properties of the foil, on the cavitation number. The next section points out the prominent differences in pressure distribution that can be identified through the 3D RANSE simulations at varying cavitation numbers.

5.2 A more detailed look at the differences in σ

The differences in cavitation number affect the point at which the inception of cavitation occurs. A larger difference between the ambient pressure and the vapor pressure of water requires a larger velocity to produce low pressure regions (through the Bernoulli effect, or the formation of vorticies for example) strong enough to induce cavitation.

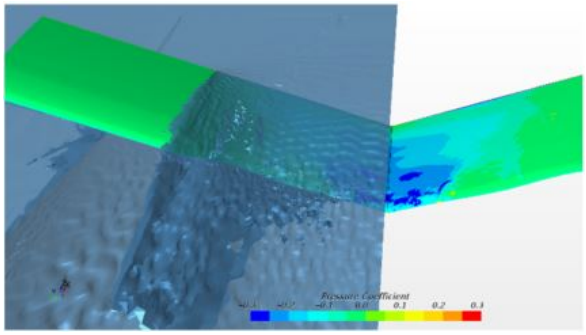

Figure 20: The disturbance of the free-surface and the pressure distribution along the back of the foil in the $\sigma_0 = 2.37$ simulation.

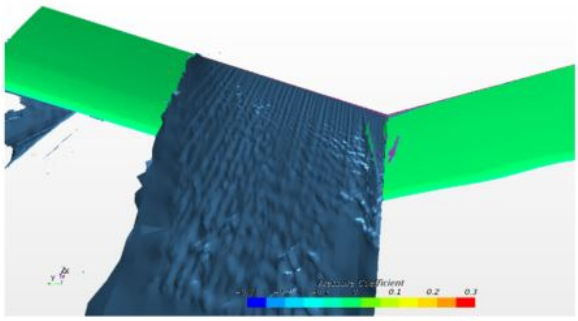

Figure 21: The disturbance of the free-surface and the pressure distribution along the back of the foil in the $\sigma_0 = 0.05$ simulation.

This effect can be observed by comparing the relative areas of ventilation along the back of the foils in each of the simulations run at different cavitation numbers. The back of the foil from the $\sigma_0 = 2.37$ simulation, shown in Fig.20, has a short region of ventilation near the free-surface. This region is identified by the disturbed free-surface on the left side of the foil image, and perhaps more easily by the green region of the foil on the right side. The green color indicates a pressure on the foil surface equal to ambient pressure. The back of the foil from the $\sigma_0 = 0.05$ simulation, shown in Fig.21, instead is ventilated along the entire area. This results from the low pressure region developed on the back of each foil only causing cavitation on the back of the $\sigma_0 = 0.05$ foil. Once this cavitation bubble grows sufficiently large, it interacts with the region of ventilation from the free-surface. This ventilation region, being at a higher pressure (p_{amb}) than the cavitation region (p_v), expands to fill the cavitation bubble, and a steady state is reached.

The higher pressure $\sigma_0 = 2.37$ run never develops a sufficiently large cavitation volume along the back of the foil, and as such, the ventilation region has no mechanism to travel down the span of the foil as in the $\sigma_0 = 0.05$ case. As a result, there is a limited region of ventilation, starting at the free-surface and going only partially down the span of the foil. The region of the foil not ventilated experiences the expected lower pressure region associated with the back of a wetted hydrofoil, but not low enough to induce cavitation.

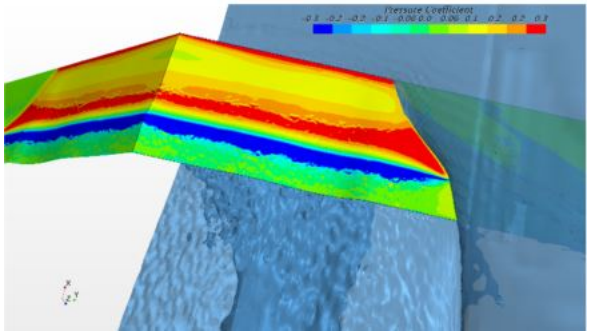

Figure 22: The disturbance of the free-surface and the pressure distribution along the face of the foil in the $\sigma_0 = 2.37$ simulation.

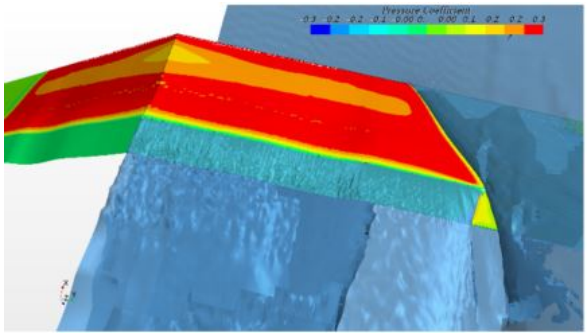

Figure 23: The disturbance of the free-surface and the pressure distribution along the face of the foil in the $\sigma_0 = 0.05$ simulation.

A similar phenomenon occurs on the face of the foil. In the higher pressure $\sigma_0 = 2.37$ simulation, on the face tail (after the kink), a low pressure region develops due to the expected vortices from flow separation. However, because of the higher static pressure, no cavitation on this section of the foil occurs. Meanwhile, in the lower pressure $\sigma_0 = 0.05$ simulation, the pressure drop is sufficient to induce cavitation. The cavitation region grows until it interacts with the ventilated region on the back of the foil. The ventilated region then crashes around the trailing edge of the foil and results in the region of the face of the foil, aft of the kink, being fully ventilated.

6 Conclusion

In this paper, we have formulated a first description of the physical mechanisms of ventilation on high speed super-cavitating, surface-piercing hydrofoils by means of experimental and computational fluid dynamics simulations. As strong coupling between cavitation and ventilation is detected and explained as a function of the cavitation number. The implications of ventilation on the simplified numerical models used for design have been discussed and relative limits of approximate models and experimental techniques given. Future versions of VLL models to predict or analyze the performance of surface piercing super cavitating hydrofoils should incorporate the lessons learned in this study. At the Froude numbers required for super-cavitating hydrofoils, a purely anti-symmetric (biplane) method of images is acceptable, a correction factor should be used to account for the disturbed free-surface, and consideration of the cavitation number to be used in operation must be considered in design. In the case of the analyzed foil cross-section, cavitation numbers below 0.1 can be considered to produce cavitation bubbles large enough to allow for full ventilation of the tail, and can be modeled as indicated above. For cavitation numbers greater than 0.1, the cavitation bubble is not sufficient to guaranteed tail ventilation, and the method used here is not acceptable. A corrected $\frac{\delta C_L}{\delta \alpha}$ curve would need to be created to determine the correct lift and drag coefficients to be expected under these conditions.

References

[1] Morrelli & Melvin Design & Engineering, Inc. (2010) *America's Cup "72" Class Rule*, Ver. 1.0.

[2] Gibbs & Cox (1954) *Hydrofoil Handbook*, Vol. I, Chap. 1.

[3] Vernengo G., Bonfiglio L., Brizzolara S. (2017) *Super-Cavitating 3D Hydrofoil Analysis by Viscous Lifting Line Approach*, accepted for publication in AIAA Journal (to be published).

[4] Prandtl, L., (1921) *Applications of modern hydrodynamics to aeronautics*, Technical Report n.116, NACA.

[5] Brizzolara, S. Bonfiglio, L, (2015) *Comparative CFD Investigation on the Performance of a New Family of Super-Cavitating Hydrofoils*, Journal of Physics: Conference Series 656.

[6] Molland A., Turnock S *Marine Rudders and Control Surfaces*, 1st edition, Butterworth-Heinemann, 2007, Chap. 5.

[7] Brizzolara, S., (2015) *A New Family of Dual-Mode Super Cavitating Hydrofoils*, Fourth International Symposium on Marine Propulsors

[8] Storn R., Price K., (1997) Journal of Global Optimization.

[9] Swales, P.D. McGregor, R.C. (1974) *Correlation of Force Measurements and Separated Flow Regions on Surface Piercing Struts*, Journal of Hydronautics, Vol. 8 No. 2.

[10] Swales P.D., Wright A.J., McGregor R.C., Rothblum R. (1974) *The Mechanism of Ventilation Inception on Surface Piercing Foils*, Journal Mechanical Engineering Science, Vol. 16, No. 1.

[11] Katz J., Plotkin A. (2001) *Low-Speed Aerodynamics*, 2nd Edition, Cambridge University Press, 2001, Chaps. 8, 12.

[12] Sivells, J.C. and Neely, R.H. (1947) *Method for calculating wing characteristics by lifting-line theory using nonlinear section lift data*, Technical Report, DTIC Document

[13] Van Dam, C. (2002) *The aerodynamic design of multi-element high-lift systems for transport airplanes.*, Progress in Aerospace Sciences, 38(2):101-144

[14] Mukherjee, R., Gopalarathnam, A., and Kim, S. W. (2003) *An iterative decambering approach for post-stall prediction of wing characteristics using known section data.*, AIAA paper, 1097:2003

[15] Anderson, J. D. (2001) *Fundamentals of Aerodynamics*, 3rd Edition, McGraw-Hill Higher Education, 2001, Chaps. 3-5.

[16] Vernengo, G., Bonfiglio, L., Gaggero, S., Brizzolara, S. (2016) *Physics-Based Design by Optimization of Unconventional Super cavitating Hydrofoils*, Journal of Ship Research, Vol. 60, No. 4, pp. 187-202

[17] ONR Grant N00014-13-1-0332

[18] Savitsky, D., Morabito, M. (2011) *Origin and Characteristics of the Spray Patterns Generated by Planing Hulls*, Journal of Ship Production and Design, Vol. 27 Issue 2, p63

[19] Auslaender J. (1962) *Low Drag Supercavitating Hydrofoil Sections*, Technical report 001-7, Hydronautics Inc. Washington D.C.